Aeroelastic Loads and Stability of Swept-Tip Hingeless Tiltrotors toward High-Speed Instability-Free Cruise

Seyhan Gul*
Graduate Research Assistant

Anubhav Datta
Associate Professor

University of Maryland, College Park, MD

A hingeless hub tiltrotor with swept-tip blades was examined comprehensively with a new rotorcraft aeromechanics solver developed at the University of Maryland. The solver was verified with hypothetical U.S. Army results and validated with Boeing Model 222 test data from 1972. A 20° sweep back from 80%R increased instability speed to 405 kt, an improvement of more than 75 kt. The key mechanism is the aerodynamic center shift. The trade-off is the increase in control system and blade loads. Fundamental understanding of physics is provided. Proprotor air resonance emerged as the critical phenomenon, not whirl flutter. Predictions in powered mode are necessary. At least the first rotor flap, lag, and torsion modes need to be included. Rotor aerodynamics should use airfoil tables; wing aerodynamics is not important for air resonance. Analysis shows high-speed flight is achievable with 13.5% thick wings but systematic wind tunnel tests with modern equipment are necessary for further validation.

Nomenclature

C_{l_α}	lift curve slope
C_{d_0}	profile drag coefficient
C_T/σ	blade loading
i_N	nacelle incidence angle, deg, 0° in airplane mode
M_x	torsional moment, $N \cdot m$
M_y	flapwise bending moment, $N \cdot m$
M_z	chordwise bending moment, $N \cdot m$
p	wing torsion mode
R	rotor radius, m
q_1	wing beam mode
q_2	wing chord mode
V	speed, kt
β	rotor collective flap mode
$\beta - 1$	rotor low-frequency flap mode
$\beta + 1$	rotor high-frequency flap mode
β_{1c}	rotor flap mode cosine component in the fixed frame
β_{1s}	rotor flap mode sine component in the fixed frame
ζ	rotor collective lag mode
$\zeta - 1$	rotor low-frequency lag mode
$\zeta + 1$	rotor high-frequency lag mode
ζ_{1c}	rotor lag mode cosine component in the fixed frame
ζ_{1s}	rotor lag mode sine component in the fixed frame
θ_{75}	collective, deg
θ_{1c}	lateral cyclic, deg
θ_{1s}	longitudinal cyclic, deg
λ_c	inflow ratio, $V\cos(i_N)/V_{\text{tip}}$
μ	advance ratio, $V\sin(i_N)/V_{\text{tip}}$
ν_ζ	rotor in-plane frequency, /rev
Ω	rotor speed, rpm

*Corresponding author; email: sgul@umd.edu.

Presented at Vertical Flight Society 77th Annual Forum, Virtual, May 10–14, 2021. Manuscript received June 2021; accepted August 2022.

Introduction

The modern tiltrotor is a versatile rotorcraft tailored for cruise at high speeds up to 270–280 kt (V-22 and V-280). One of the major barriers to achieve even higher speeds is whirl flutter or drag penalty due to the thick wings required to prevent it. Flutter of tiltrotors is a unique instability that arises with large rotors and blade flapping which are essential for good hover and helicopter mode flight. Whether the blades, hubs, or wings can be refined or altered for higher cruise speeds still remains an interesting area of research.

Hingeless hubs have the potential to achieve significantly higher speeds. Three kinds of hingeless hubs are possible: soft in-plane (lag frequency less than 1/rev), stiff in-plane (lag frequency greater than 1/rev), and hyper-stiff in-plane (lag frequency greater than 3/rev). Stiff in-plane gimballed hub is the current tiltrotor technology. Hyper-stiff hingeless hub envisions advanced, ultralight materials. Soft in-plane is a conservative approach where blade technology can remain similar. In-plane bending loads can also be alleviated. The exploration in this paper is focused on soft in-plane as it is the only data available for validation.

Hingeless hubs may have better flutter characteristics and lighter weight than their gimballed counterparts despite the increase in flap bending moments in helicopter mode. A tiltrotor aircraft with a hingeless hub was identified by NASA Heavy Lift Rotorcraft Systems Investigation as having the best potential to meet the technology goals for large civil transport (stiff in-plane; Ref. 1). Karem Aircraft's design for Joint Multi

DOI: 10.4050/JAHS.68.012001

Role demonstration also utilized a hingeless hub tiltrotor (hyper stiff in-plane; Refs. 2, 3). None of these aircraft were built or tested in model scale; hence, a thorough understanding of whirl flutter and air resonance characteristics of hingeless hubs is acutely missing. The purpose of this research is to bridge this gap, starting with analysis.

There have been a very limited number of hingeless hub proprotor tests. These are 1/4.622 and 1/9.244 Froude-scale and full-scale Boeing M222 tests in the 1970s. All these rotors had soft in-plane hubs.

A 1/4.622 Froude-scale full-span model of the Boeing M222 rotor was built and tested in the Boeing V/STOL wind tunnel in 1976 (Ref. 4). Parametric blade, pitch link, hub, and airframe loads for different tunnel speeds, nacelle tilt angles, collective and cyclic pitch controls, wing flap angles, and aircraft attitudes were collected. The primary objective was to provide the basis for understanding the rotor and airframe behavior of this aircraft. A secondary objective was to examine the feasibility of a control system to minimize the rotor loads by changing the blade control angles and providing control using aircraft control surfaces in cruise. Whirl flutter was not investigated.

A 1/9.244 Froude-scale model of the Boeing M222 rotor was tested in the MIT Wright Brothers tunnel (Refs. 5, 6). The primary objective was to determine the response to vertical and longitudinal gusts. Different gust frequencies were tested but only at a single tunnel and rotor speed. Neither whirl flutter nor loads were investigated.

The most important data on a hingeless hub proprotor were acquired almost 50 years ago by the full-scale Boeing M222 tiltrotor tests in NASA Ames 40-ft $\times$ 80-ft wind tunnel in 1972 (Ref. 7). The objectives were to investigate the rotor/pylon/wing aeroelastic behavior and to measure blade and control loads, stability derivatives, and performance. However, these tests were limited, only one set of blades (straight, twisted) was used. More importantly, the tunnel speed was too low for any instability at the design rotor speed. With industry focus shifting to gimballed hubs, no further tests were conducted on the hingeless hubs. Today, with materials, controls, and simulation capabilities improved dramatically, there still remains a dearth of knowledge on hingeless hub proprotors.

Some important analytical work has been published in recent years. Yeo and Kreshock (Ref. 8) investigated whirl flutter characteristics of hypothetical hingeless hubs with various blade frequency and aerodynamic options and established code-to-code consistency among CAMRAD II (Comprehensive Analytical Model of Rotorcraft Aerodynamics and Dynamics II; Refs. 9, 10) and RCAS (Rotorcraft Comprehensive Analysis System; Refs. 11, 12). This work did not include any analysis for swept-tip blades but provided important verification results for straight, twisted blades as will be explained later.

Bowen-Davies carried out an analysis of the M222 proprotor loads in hover, transition, and cruise with various wake models (Refs. 13, 14). Reference 13 also explored air resonance but only to validate the RCAS model; design variations or modeling refinements were out of scope.

The emphasis of this work is on swept-tip blades. The authors are inspired by Acree's work (Refs. 15, 16) on the advantages of the swept-tip blades on gimballed hub tiltrotors. The objective is to examine the impact of swept-tips on hingeless hub tiltrotors. However, these rotors can display different kinds of instability characteristics. Thus, it is important to first understand the nature of the instability and the fundamental mechanisms that impact it.

Scope

In order to study the stability mechanisms from the first principles, a new aeromechanics solver was developed. The solver was named UMARC-II. The predictions were first verified with the unique hypothetical problem created by the U.S. Army. Next, available test data and properties were consolidated from the Boeing full-scale test for validation. The validated solver was then used to systematically identify the nature of hingeless hub instabilities and the key mechanisms that are fundamental to predict them. These are described in the sections on validation and fundamental understanding, respectively. Finally, the essential modeling elements that capture the key mechanisms were used to understand the impact of swept-tip blades.

Aeromechanics Solver

Special features are required to predict the blade and hub vibratory loads and stability roots of a tiltrotor aircraft. This means accurate structural and aerodynamic models with no small angle or small inflow assumptions as well as the incorporation of hub motions through flexible wing and pylon that couple with the rotor. The new solver, UMARC-II, meets these requirements with finite element blades, wing, pylon, multibody joints, freewake, a fixed–rotating interface, and solution procedures for trim, transient, and stability in both frequency and time domains. UMARC-II departs from UMARC (Ref. 17) with its numerical extraction of aerodynamic and inertial terms which eliminates small-term assumptions, its generic fixed–rotating interface, and multibody joint modeling. A summary of the solver is given below. Theory for the key features is reported in Ref. 18.

Structural model

The structural model uses isotropic beams and multibody joints that exhibit deformations in flap, lag, axial, and torsion. Deformations can be moderate as the model includes nonlinearities up to second order. Some higher than second-order structural terms that are important particularly for hingeless proprotors are retained. These are multiplication of flap and lag curvature and elastic twist terms which govern the coupling of flap and lag motions. Inertial terms are obtained exactly by numerical perturbation with no small term assumption; hence, an ordering scheme is not used. A Taylor series expansion is used to linearize the inertial loads about deflection, slope, and corresponding velocity and accelerations. Advanced geometry blades are modeled by sweeping and drooping the elastic axis, which is taken into account with inter-segment boundary conditions and elastic axis positions. Fixed–rotating interface can be implemented for any geometry. The wing and the pylon can be modeled directly and coupled with the rotor, or frequency and mode shape inputs for the fixed structure can be admitted.

The structure is modeled with long and slender Euler–Bernoulli beams with linear isotropic materials. The equations of motion were adapted from Hodges and Dowell (Ref. 19), which has been validated with UH-60A flight test data in Refs. 20 and 21, and references therein. The elastic axial deformation is treated as quasi-coordinate (Ref. 22) with the option to use the total axial deformation that makes modeling of multiple load paths easier.

The Hamilton's principle with finite element discretization is used to obtain the governing ordinary differential equations. Each finite element is straight and has 15 degrees of freedom, 12 of which are at the boundaries. The boundary degrees of freedom can be eliminated when connected to joints or other beam elements. Axial and torsion deformations use third- and second-order Lagrange polynomials, respectively, as shape functions (for continuity of displacement) while flap and lag deformations use third-order Hermite polynomials (for continuity of displacement and slope). The inputs are cross-sectional stiffness EI and GJ; mass, moment of inertia; center of gravity, tension center, quarter-chord offsets; pretwist, sweep, anhedral angles; and joint actuation and connection to the elements. These are specified as a function of span and

Table 1. Generic NASTRAN wing/pylon frequencies and mode shapes at the rotor hub

Mode	Frequency (Hz)	X[a]	Y[a]	Z[a]	θ_X[b]	θ_Y[b]	θ_Z[b]
Wing beam	3.43	0.000	0.000	−2.673	−0.025	−0.015	0.000
Wing chord	6.83	−2.024	−1.593	0.000	0.000	0.000	0.033
Wing torsion	8.63	0.000	0.000	3.954	−0.020	0.116	0.000
Pylon yaw	14.67	−0.720	4.480	0.000	0.000	0.000	−0.093

[a]Unit: $\sqrt{\text{in}}/\sqrt{\text{lbf s}^2}$.
[b]Unit: $\text{rad}/\sqrt{\text{lbf s}^2\ \text{in}}$.

can vary along an element. A six-point Gaussian quadrature integration is used for each element.

Aerodynamic model

Unsteady lifting-line theory is used for aerodynamics. Sectional angles of attack are calculated exactly from flexible blade deformations and hub motions. Aerodynamic stiffness and damping matrices are extracted by numerical perturbation; hence, nonlinear C81 airfoil decks can be used. Large inflow and hub motions important for tiltrotor stability are taken into account exactly and generally for any rotor/pylon/wing attachment. Radial flow corrections for the swept part of the blade are included (Ref. 23). The Maryland Freewake can be used with a full-span near-wake model. Freewake is essential in helicopter mode transition flight. In high-speed cruise, it is inconsequential and in fact the least important piece of the model. Wake is quickly washed away from the rotor; wake distortion is not important, and a uniform inflow assumption suffices as long as high inflow is accounted for exactly in the section angles of attack. Wing aerodynamics is also modeled with the same fidelity.

Trim and transient solution

The final state equations are solved with the finite element in time (FET) for direct extraction of periodic steady-state or time marching for full transient. FET is fast and efficient for a trim solution; hence, it was used for all the predictions in this paper. The rotor equations are solved in the rotating frame, and the wing/pylon equations are solved in the fixed frame in a fully coupled manner. The periodic solution can be used as an initial condition for the stability or transient solution with arbitrary time-varying control inputs.

Stability

The stability of the rotor/pylon/wing system is determined first by trimming the system using FET and then applying numerical perturbation to extract the mass, stiffness, and damping matrices due to aerodynamic and inertial forces. A constant coefficient approximation is used as it is valid and accurate for airplane mode axial flight. Stability roots can be obtained either in the rotating frame or in the fixed frame after applying a numerical multiblade coordinate transformation.

Available Data and Properties

There is a scarcity of validation data for the stability of hingeless hub proprotors. U.S. Army's recent hypothetical test case results with CAMRAD II and RCAS (Ref. 8) provided valuable data for verification. The Boeing M222 tests provided the only available validation data for stability. Although the rotor was tested up to 192 kt which was far away from flutter, the tip speed was varied at tunnel speeds from 50 to 192 kt until proprotor air resonance behavior was observed. However, because of the low tunnel speed, a comprehensive understanding of the stability envelop could not be provided by these tests. In addition, the properties of this rotor in the public domain are incomplete and ripe for misinterpretation. Until further test data are available, the Boeing M222 tests provided the only anchor point for hingeless hub proprotor stability predictions.

Table 2. U.S. Army hypothetical soft in-plane hingeless rotor properties

Number of blades	3
Radius	4 ft
Chord	0.5 ft
Precone	2.5°
Twist	−40°
Rotor speed	742 rpm
Flap frequency	1.19/rev
Lag frequency	0.76/rev
Torsion frequency	7.49/rev

Verification with U.S. Army Hypothetical Case

The present analysis was verified with the recent hypothetical U.S. Army case. Rotor models that exhibit different flap, lag, and torsion frequencies were combined with a simple rigid pylon with root springs and a generic NASTRAN wing/pylon model. In the Army paper (Ref. 8), the NASTRAN wing/pylon was modeled with frequency and mode shape inputs to the comprehensive analysis. In the present work, the model was built into the University of Maryland (UMD) solver instead of direct inputs and coupled with the rotor. Frequency and mass-normalized mode shapes of the NASTRAN wing/pylon are given in Table 1. The terms X, Y, and Z denote translations at the rotor hub, and θ_X, θ_Y, and θ_Z denote rotations. Table 2 shows principal rotor characteristics.

First, periodic solution was obtained for freewheeling condition. Next, the mass, stiffness, and damping matrices were calculated by numerical perturbation and a multiblade coordinate transformation was performed. Figure 1 shows UMD frequency and damping predictions for the generic NASTRAN wing/pylon combined with the soft in-plane rotor and a comparison with CAMRAD II and RCAS. The modes are labeled as follows: q_1 is wing beam mode, q_2 is wing chord mode, $\beta - 1$ is low-frequency flap mode, and $\zeta - 1$ is low-frequency lag mode. Wing chord (q_2) mode goes unstable at 80 kt. Although some discrepancy exists in the $\zeta - 1$ frequency predictions at high speeds, the damping values show excellent agreement. The instability speed is also accurately predicted.

Validation with Full-Scale Boeing M222 Test

A full-scale Boeing M222 rotor was tested in NASA Ames 40-ft × 80-ft wind tunnel in 1972. Two types of tests were conducted: unpowered (freewheeling) rotor on two vertically mounted semispan wings (full-stiffness and quarter-stiffness NASA dynamic wing test stands; Fig. 2(a)) and powered rotor on an isolated propeller test rig (Fig. 2(b)). Loads,

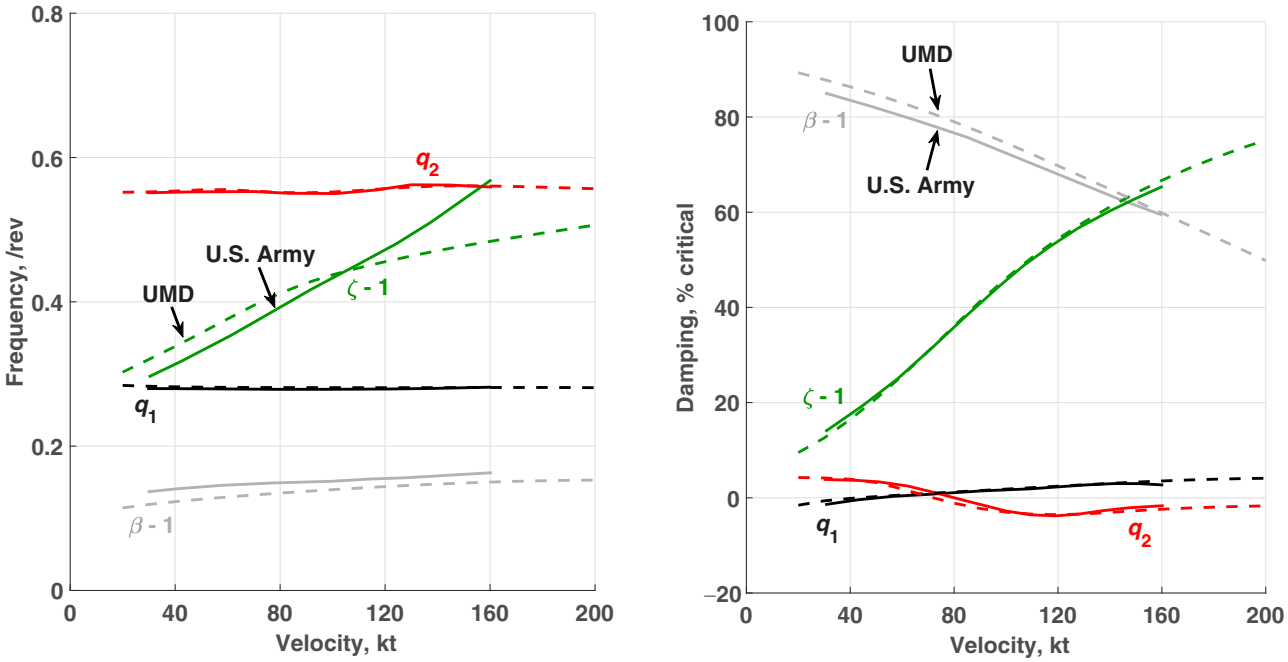

(a) Frequency (b) Damping

Fig. 1. Aeroelastic stability verification for generic wing/pylon and soft in-plane hingeless rotor (solid: U.S. Army predictions with CAMRAD II and RCAS (Ref. 8), dash: UMD predictions with UMARC-II).

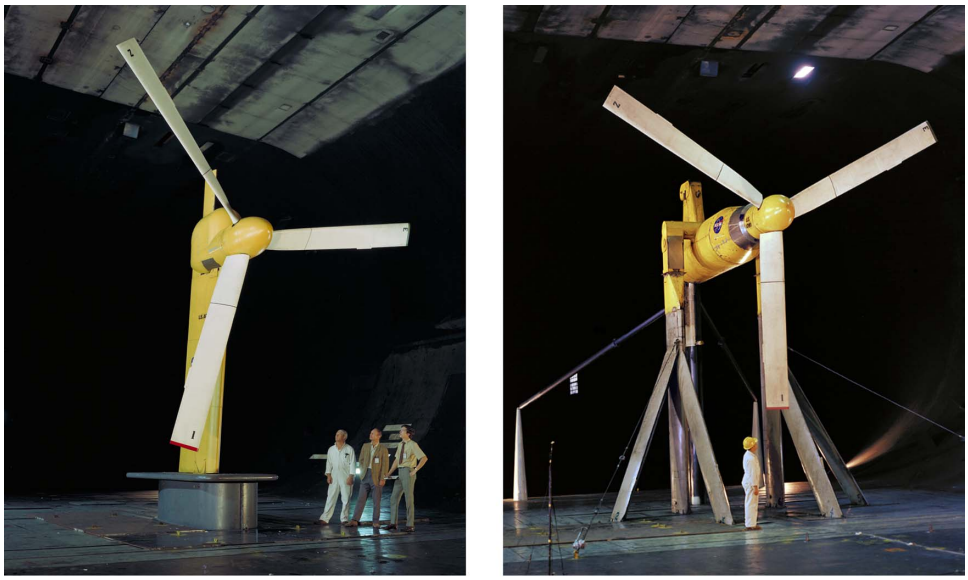

(a) Mounted on NASA dynamic wing test stand (b) Mounted on NASA powered propeller test rig

Fig. 2. Boeing M222 tests in NASA Ames 40-ft × 80-ft wind tunnel (1972).

performance, and stability of the rotor/pylon/wing system were measured. Only a portion of the performance and loads validation is given in this paper; the complete study can be found in Ref. 18. Principal characteristics of the rotor and the wing are given in Tables 3 and 4. The test points are shown in Table 5.

The stability of the rotor/pylon/wing system was measured at multiple rotor and tunnel speeds but only up to 192 kt (200 kt was the maximum speed of the 40-ft × 80-ft tunnel at the time). The purpose of testing the rotor on the quarter-stiffness wing, which exhibited half the natural frequencies of the full-stiffness wing, was to simulate an inflow ratio equivalence of 400 kt (the rotor operated at half the design rotation speed). However, the simulation of the blade frequencies was not satisfactory at this rotor speed due to the first bending frequency (lag mode) being close to 1/rev. This not only had an influence on the dynamics but also meant large vibrations and blade loads. The model was excited with a shaker vane mounted outboard of the nacelle which could oscillate at various amplitudes and at frequencies ranging from 2 to 20 Hz. Two sets of strain gauges were installed on the wing: one set near the root to measure flap bending, chord bending, and torsion moments and another near the tip to measure chord bending moment, torsion moment, and

Table 3. Boeing M222 rotor properties

Number of blades	3
Radius	13 ft
Chord	1.57 ft
Precone	2.5°
Torque offset	0.65 in (lead)
Solidity	0.115
Twist	−41°
Rotation direction	counterclockwise
Rotor speed – helicopter	551 rpm
Rotor speed – airplane	386 rpm
Airfoil (10%R)	NACA 23021
Airfoil (45%R–100%R)	Boeing-Vertol 23010-1.58
Swashplate phase angle	20°

Table 4. Full-stiffness NASA dynamic wing test stand properties

Span	165 in
Thickness	13.5%
Chord	5.17 ft
Beam frequency, damping	2.5 Hz, 1%
Chord frequency, damping	4.5 Hz, 0.64%
Torsion frequency, damping	11.3 Hz, 1.74%

Table 5. Boeing M222 test points

Test	Run	Condition	V (kt)	i_N (deg)	Ω (rpm)	M_{tip}
416	6	Hover	0[a]	0	var	var
416	7, 15	Hover	0[a]	0	551	0.67
416	16	Shutdown	0[a]	66	var	var
416	19	Transition	45	85	500	0.61
416	22	Transition	76	83	500	0.61
416	21	Transition	80	66	550	0.67
416	20	Transition	80	66	500	0.61
416	9[b]	Transition	105	27	551	0.67
416	13	Transition	140	27	551	0.67
416	11	Cruise	140	10	386	0.47
416	14	Cruise	170	10	386	0.47
410	(3–7)[b]	Freewheeling	50	0	var	var
410	8[b]	Freewheeling	60	0	var	var
410	(9, 10)[b]	Freewheeling	100	0	var	var
410	(12, 17)[b]	Freewheeling	140	0	var	var
410	(14, 15)[b]	Freewheeling	192	0	var	var

[a]Effectively in climb due to tunnel recirculation.
[b]Conditions analyzed.

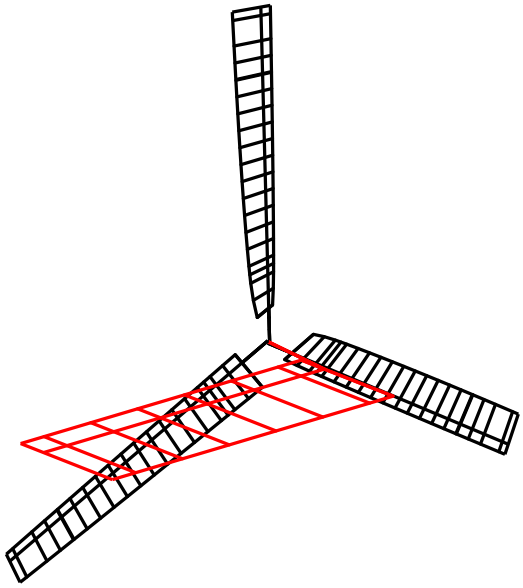

Fig. 3. UMARC-II model of the Boeing M222 tiltrotor (rotor, pylon, and wing are beams, panels show aerodynamic segments).

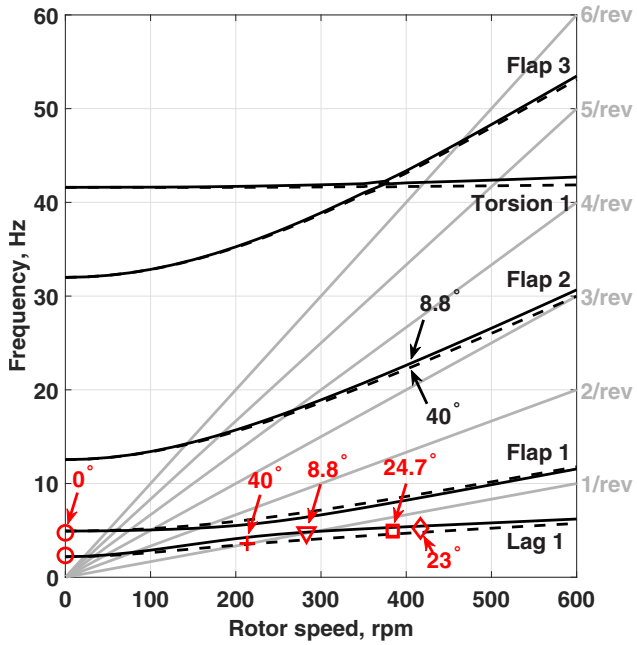

Fig. 4. Boeing M222 fanplot (solid: predictions for 8.8° collective, dash: predictions for 40° collective, symbols: test data).

normal and chordwise forces. Flap and chord bending moments along the blade were measured at multiple spanwise locations. Control loads were collected on a pitch link and the longitudinal actuator ground point bolt. One historical importance of this test is that Bell Model 300 rotor with a gimballed, stiff in-plane hub was also tested in the same wind tunnel and with the same wings. Therefore, this test marked the first interchangeable hub tiltrotor wind tunnel test.

The rotor/pylon/wing model built in the present solver is shown in Fig. 3. The full-stiffness wing was modeled. The wing/pylon model uses orthogonal frequency and mode shape inputs along the wing span, pylon, and hub, as reported in Ref. 7. The model uses 10 elastic rotor modes, uniform inflow, and freewake model, and appropriate airfoil decks for both the rotor and the wing. The rotor airfoil decks were obtained with in-house two-dimensional CFD—TURNS. Linear interpolation was used for the airfoil transition region (10%R–45%R). Stability results were obtained in freewheeling mode operation. Freewheeling means unpowered, hence allows rotor speed perturbation. This model was built with the properties given in Refs. 13 and 24.

Figure 4 shows the rotor frequencies together with the test data. Predictions are shown for 8.8° (solid lines) and 40° (dashed lines) collective angles. Test data are shown for 0°, 8.8°, 23°, 24.7°, and 40° collectives. The nonrotating and rotating frequencies are accurately predicted.

Freewheeling

Stability tests were carried out in freewheeling condition (test 410). This is typical of whirl flutter tests, as freewheeling decouples special

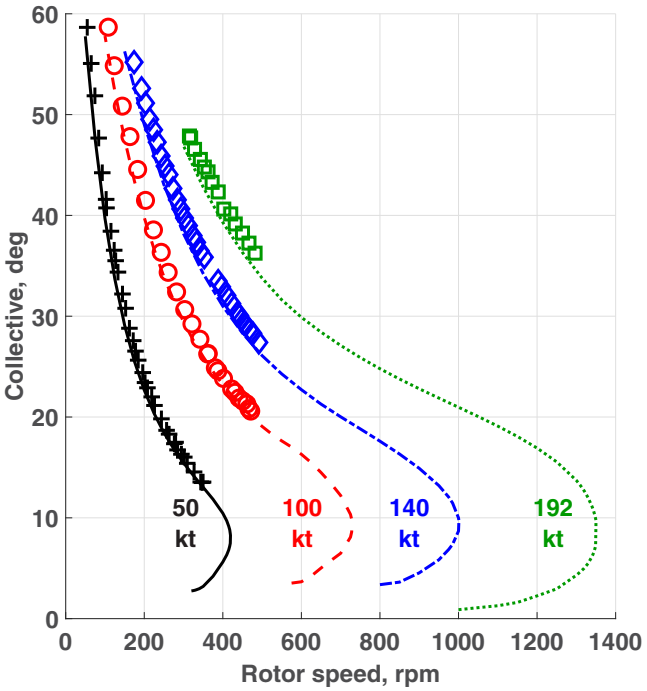

Fig. 5. Comparison of freewheeling collective predictions with Boeing M222 test data (lines: predictions, symbols: test data).

features of the drivetrain, and also generally results in conservative whirl flutter boundary while achieving near representative collective as powered flight. Testing in freewheeling mode also reduces the complexity of the test that may arise due to powerplant stalling. Accurately predicting the rotor speed versus collective at a given tunnel speed is crucial for whirl flutter because of the effect of blade pitch angle on the coupling of flap and lag modes.

Figure 5 shows a comparison of the freewheeling predictions with the test data. The lower side of Fig. 5 below 10° collective shows reverse stall. Boeing tests have no data there because the higher side is more representative of the actual flight. Some small offset is observed for higher pitch settings, but there is generally a good agreement considering that the performance validates gross characteristics. The next step is to validate the structural loads.

Blade loads

Structural loads on the blades were measured in hover, transition, and cruise. The tests were performed by keeping two out of three rotor controls (collective and cyclics) constant and varying the other in a set flight condition (defined by tunnel speed, incidence angle, and rotor speed). Blade loads were recorded in directions normal and parallel to the local chord except for the hub barrel gauges at $r/R = 3.9\%$, where the loads were measured in out-of-plane and in-plane directions. This paper only includes transition loads; a detailed loads validation study including various nacelle incidence angles, rotor speeds, and tunnel speeds can be found in Ref. 18.

The loads analysis was carried out both using the reported control angles (solid lines) and trimming to the hub moments (dotted lines). The Maryland Freewake was used with a single tip vortex and a nearwake extending 30° behind. Induced flow and wake geometry were converged for each solution.

Transition generates high oscillatory loads which dominate the structural design. Figure 6 shows the variation of half peak-to-peak flapwise and chordwise bending moments with respect to lateral cyclic for a 105-kt transition run (test 416, run 9). The collective and longitudinal cyclic were $\theta_{75} = 18.9°$ and $\theta_{1s} = -2.56°$. The general trends were predicted, but some difference in the magnitudes is present. Offset in the cyclic values is observed. Similar observations and offset values (changing between 0.66° and 1.12° with different methods) were reported in Ref. 14, where the loads were calculated with vortex wake, viscous vortex particle method (VVPM) (Refs. 25, 26), and Helios™ (CFD) (Ref. 27). The magnitudes of the minimum loads were predicted more accurately with the hub load trim. The minimum loads point is due to the edgewise flow component; there exists a set of cyclics that alleviate the oscillatory loads because of the edgewise flow. The differences can be due to measurement errors, incorrect model properties, or errors in the analysis. It is difficult to pin down without high-quality data and consistent properties. In general, sufficient confidence in the accuracy of the loads predictions could be established in order to proceed to more involved aeroelastic stability validation.

Aeroelastic stability

First, the physical phenomenon is explained. The predictions are shown with respect to airspeed in Fig. 7. Uniform inflow was used for the rotor for both freewheeling trim and stability analysis. Wing aerodynamics did not include an induced flow model for simplicity. The modes are labeled with the dominating degree of freedom. After an initial drop in the wing chord (q_2) mode damping at around 150–200 kt due to coupling with the collective lag (ζ) mode, it is stabilized at higher speeds. Wing beam (q_1) mode is stable for all the flight speeds. After 250 kt, damping of the wing torsion (p) mode decreases precipitately and goes unstable at 327 kt. This is the proprotor air resonance phenomenon that occurs due to the soft in-plane hub ($\nu_\zeta < 1/\text{rev}$). An in-plane motion is generated at the rotor hub due to the wing torsion (p) motion and this couples with the low-frequency lag ($\zeta - 1$) mode. Figure 8 shows the time vector representation of this mode at 50 and 325 kt. The eigenvector set for a given mode rotates counterclockwise at the damped frequency and the magnitudes decrease exponentially at a rate determined by the damping ratio. The projection of each line on the real axis gives the participation of the corresponding degree of freedom during the damped oscillation of the system. The terms β_{1c} and β_{1s} are the flap degrees of freedom; ζ_{1c} and ζ_{1s} are the lag degrees of freedom in the fixed frame. The wing torsion (p) mode is coupled with wing beam (q_1) mode for all speeds due to high pylon mass (2000 lb without blades) and pylon c.g. offset (10.8 in (6.9%R) forward of wing elastic axis), but mostly assumes a lag mode shape (dominant ζ_{1c} and ζ_{1s}) near instability (Fig. 8(b)). Both whirl flutter and proprotor air resonance are results of the coupling of rotating and fixed structure modes. However, air resonance is driven by rotor lag motion and occurs at the frequency of the low-frequency lag mode, whereas whirl flutter is due to coupling of rotor flap and wing modes and occurs at the wing frequencies. Collective lag (ζ) mode damped frequency is zero after 325 kt because this mode reaches 100% damping that is not visible in the damping plot.

Figures 9 and 10 show the test data and predictions with respect to rotor speed at various tunnel speeds. Frequencies are reported for 100 kt to show the coupling of the modes. Damping results are presented for the q_1 mode as the test data are only available for this mode. Also shown for comparison are the damping predictions from Ref. 13 (dotted lines) for additional verification. These were obtained using the measured modal damping given in Table 4 instead of a wing aerodynamic model. A simplified set of predictions that used the same modal damping values is therefore also included in the damping plots (dashed–dotted lines)

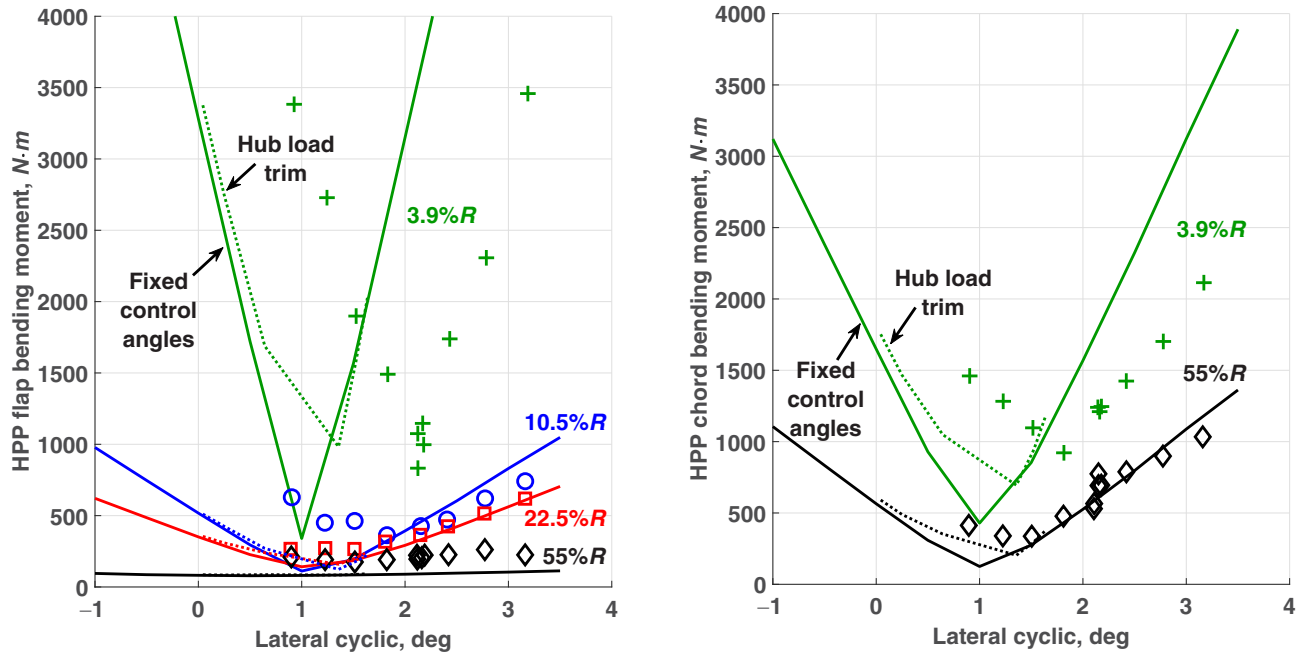

(a) Flapwise (b) Chordwise

Fig. 6. Comparison of 105 kt transition alternating bending moment predictions with Boeing M222 test data ($\mu = 0.11$, $\lambda_c = 0.21$, $i_N = 27°$ from the flow) (solid: predictions with control angles, dot: predictions with hub load trim, symbols: test data).

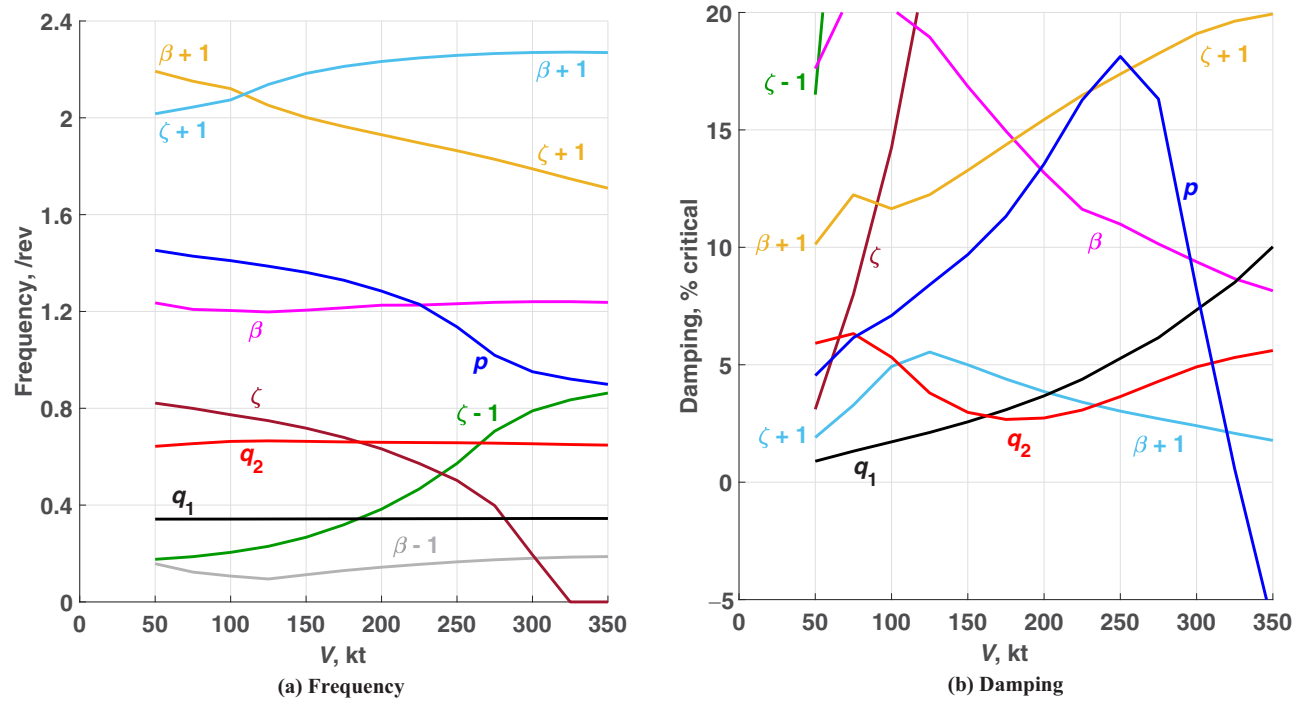

(a) Frequency (b) Damping

Fig. 7. Stability roots of coupled modes at the designed rotor speed (386 rpm).

to compare the predictions with Ref. 13. In reality, wing aerodynamic damping increases with the tunnel speed; hence, one set of values cannot be valid for every test speed.

Figure 9 shows that damping of the q_1 mode first exhibits some change near 200 rpm when it is coupled with the $\beta-1$ mode and then decreases dramatically at around 450 rpm. This is again the proprotor air resonance, this time due to the coupling of the $\zeta-1$ and q_1 modes. The test data should be compared with the predictions that model proper wing aerodynamics. The agreement is satisfactory for low speeds, but some offset is observed for the damping at 140 and 192 kt. The instability at 100 and 192 kt was not captured at all although the behavior for 100 kt was generally predicted. The discrepancies might be attributed to inaccurate

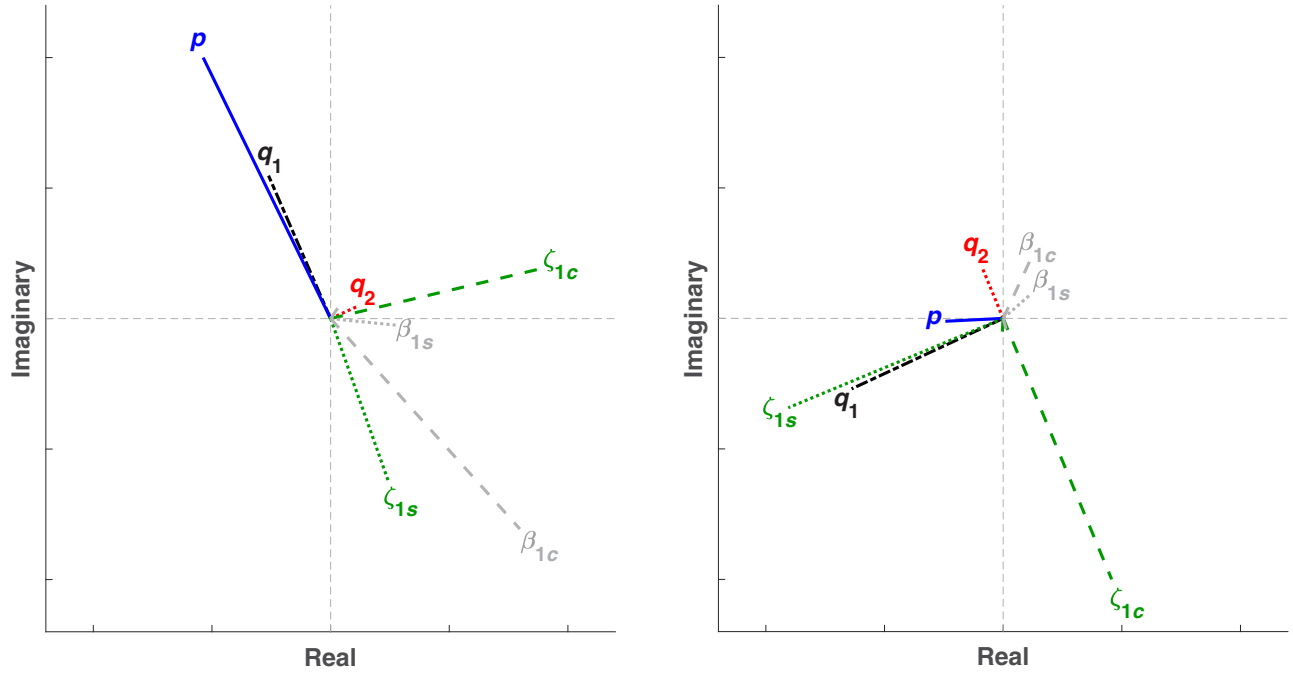

(a) 50 kt (b) 325 kt

Fig. 8. Eigenvectors for the wing torsion mode.

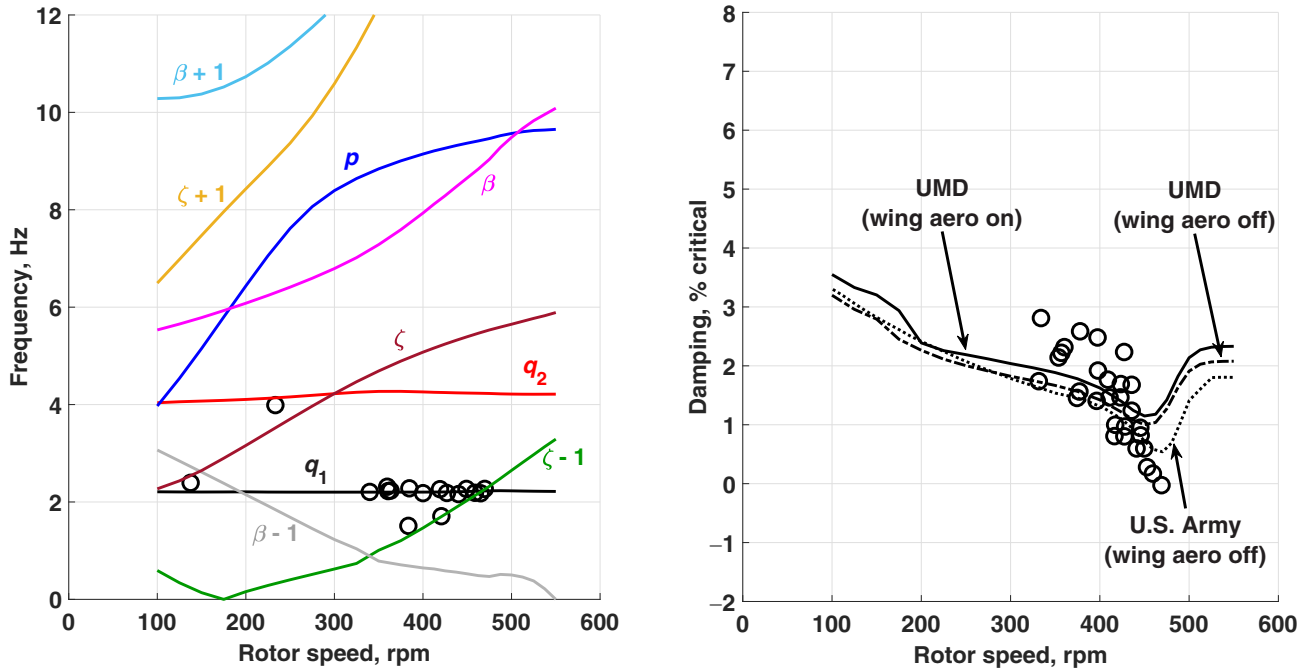

(a) Frequency (b) Wing beam mode damping

Fig. 9. Stability roots of coupled modes at 100 kt (lines: UMD (UMARC-II) and U.S. Army (RCAS; Ref. 13) predictions, symbols: test data).

modeling of physics, incorrect model inputs, or possible measurement uncertainties with the equipment used in the 1970s, but the cause remains unknown. An interesting behavior is that even though the drop in the damping is still present, the q_1 mode is stabilized as the tunnel speed increases due to higher aerodynamic damping in rotor lag and wing beam motions, but only until 192 kt (Fig. 10). At 192 kt, the damping data show an unexpected decrease. This trend was captured neither by UMD nor by RCAS.

Generally, UMD and RCAS predictions agree well with each other when modal damping is used. The highest discrepancy is for 100 kt

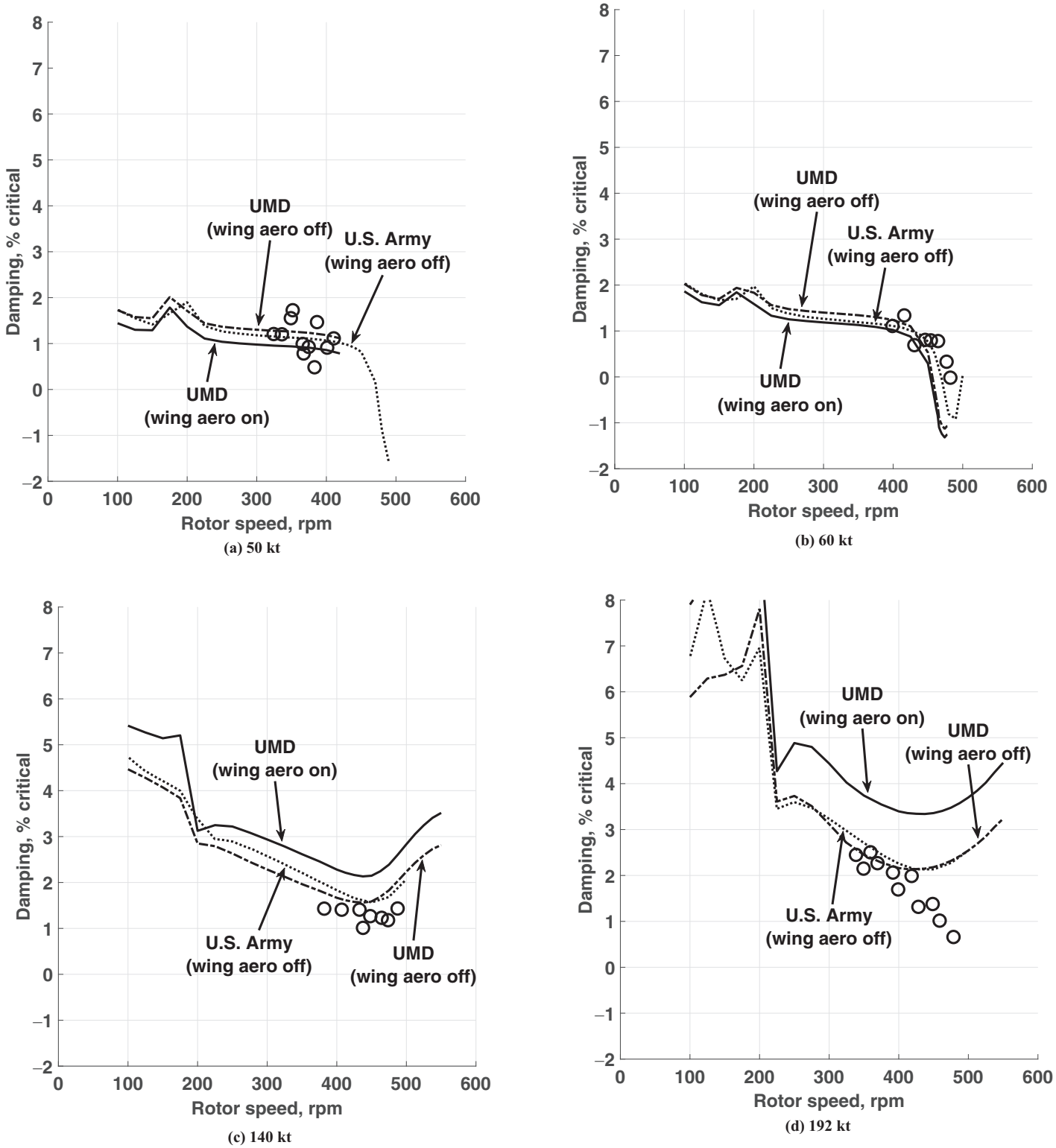

Fig. 10. Wing beam mode damping (lines: UMD (UMARC-II) and U.S. Army (RCAS; Ref. 13) predictions, symbols: test data).

(Fig. 9(b)), where a maximum 0.7% difference in the damping and 20 rpm in the air resonance rotor speed is observed. The sources of the small differences between the two sets of predictions are not clear. UMD predictions with wing aerodynamics and modal damping show similar results for 100 kt, which verifies the wing aerodynamic model. Higher damping values were predicted for 140 and 192 kt with a wing aerodynamic model, which is expected. The predictions for 50 and 60 kt do not reach as high rotor speeds as RCAS because the rotor achieves maximum speed before stalling as shown in Fig. 5.

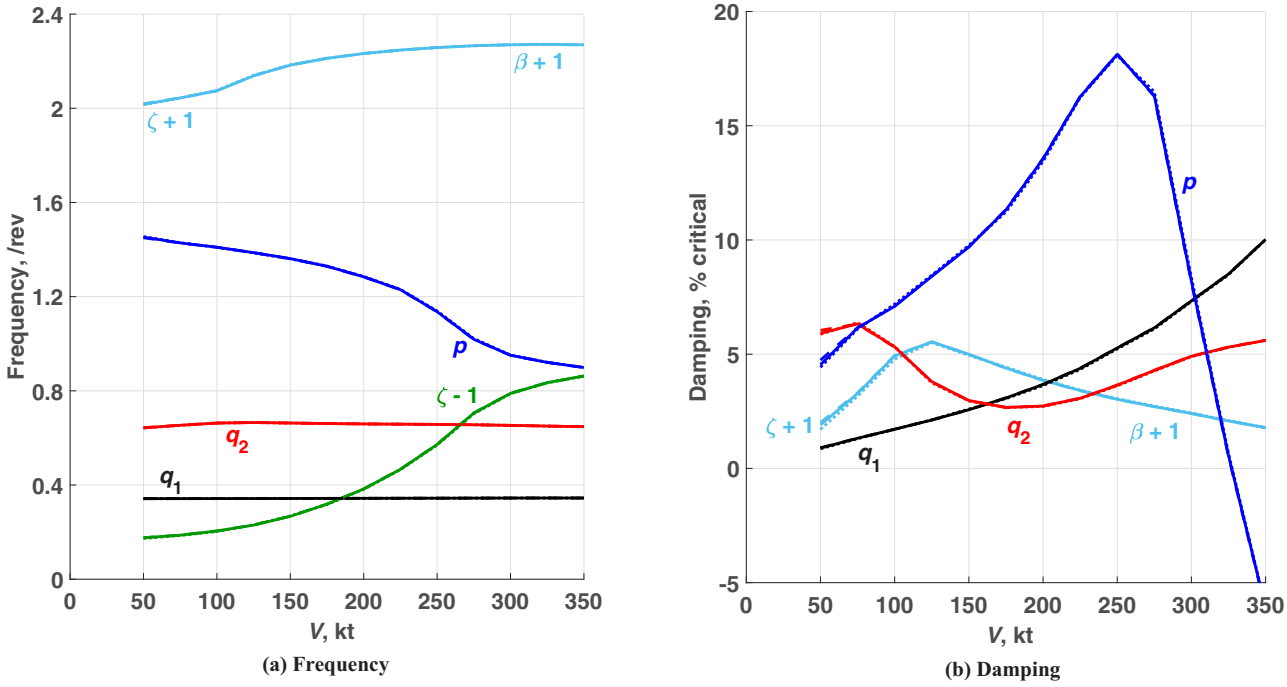

(a) Frequency (b) Damping

Fig. 11. Effect of induced flow (solid: uniform inflow - baseline, dash: no induced flow, dot: Maryland Freewake).

Fundamental Understanding

This section presents a sensitivity analysis of stability predictions to model complexity. It is aimed at establishing modeling and testing requirements and shedding further light on the physical phenomena. The highly damped rotor modes are not included in the figures for readability. The following are studied one by one: (1) effect of induced flow model, (2) effect of rotor speed perturbation and powered mode operation, (3) effect of rotor modes, (4) effect of blade airloads model, and finally (5) effect of wing aerodynamics.

Figure 11 shows the effect of the rotor induced flow model. Freewake geometry was converged for the trim solution and kept constant as the states were perturbed for the stability solution. This is because the change of trailed vorticity due to perturbation of states is insignificant. Shed vorticity, on the other hand, may be significant which was taken into account with unsteady lifting-line theory for all the induced flow models. Figure 11 shows that the predictions with uniform inflow, no induced flow, and freewake with a single free tip vortex and with full-span nearwake are almost indistinguishable. This is because the induced flow is insignificant compared to the flight speed, and the wake is quickly washed away from the rotor in high-speed flight. The inflow ratio (λ_c) varies from 0.16 to 1.12 from 50 to 350 kt.

Figure 12 shows the effect of rotor speed perturbation and powered mode operation. The dashed lines removed the joint at the rotor hub (in rotation direction), but the rotor still operates in freewheeling mode. The dotted line, in addition to removing the joint, also took into account the actual flight of the Boeing M222 aircraft by considering the parasite drag at the corresponding flight speed; a flat plate area of 6.279 ft^2 was used based on Ref. 28, and the rotor was trimmed to produce half of this drag (two rotors on the aircraft). When the engine is considered ideal (dashed lines), which is perhaps closer to an electric drive, damping of q_1 mode increases compared to the baseline but p mode stays mostly unaffected. When the rotor is also trimmed in powered mode (dotted lines), an interesting behavior is observed for air resonance. Coupling of $\zeta-1$ and p modes becomes more dominant; as a result, the damping of the p mode drops much earlier. This is one of the fundamental differences of soft in-plane hingeless hub tiltrotors from their stiff in-plane gimballed counterparts where air resonance is not observed. These predictions show that it is important to perform stability predictions for both freewheeling mode with rotor speed perturbation and powered mode for these kinds of hubs. The most conservative results can then be used for design or testing purposes.

Figures 13 and 14 show the effect of rotor modes. The solver can apply modal reduction by taking into account a set number of modes for the rotor and the wing. Using only the first three rotor modes (flap, lag, and torsion) resulted in relatively close air resonance predictions to the baseline model where 10 rotor modes were used. The highest difference is in $\beta + 1$ mode. When the torsion mode was removed, significantly higher p damping was predicted at high speeds (coupling of $\zeta - 1$ and p modes is delayed). This is mostly because the rotor torsion deflection has a direct effect on the collective angle required to trim the rotor, which in turn introduces coupling between rotor flap and lag modes. Obviously, using only the rotor flap mode (Fig. 14) did not capture air resonance at all.

Figure 15 shows the effect of the blade airloads model. Simplifying the model by replacing the airfoil tables with a linear aerodynamic model that used $C_{l_\alpha} = 5.73$, $C_{d_0} = 0.01$, and the Glauert correction for compressibility (dashed lines) resulted in significantly higher damping for p mode at high speeds again due to delayed coupling of the modes. Removing the Glauert correction (dotted lines) predicted even higher damping for p mode. Airfoil decks seem necessary for the correct prediction of the proprotor air resonance instability. This means numerical perturbation is required; simple analytical equations should not be used.

Figure 16 shows the effect of the wing aerodynamic model. As expected, using incompressible linear aerodynamics changed the high-speed predictions for the q_1 mode, but not significantly. The most important conclusion here is the necessity of a wing aerodynamic model if q_1 is the critical mode. When it is omitted, this mode has significantly lower damping. This may result in too conservative stability predictions. In such a case, wing aerodynamics should use the correct airfoil decks

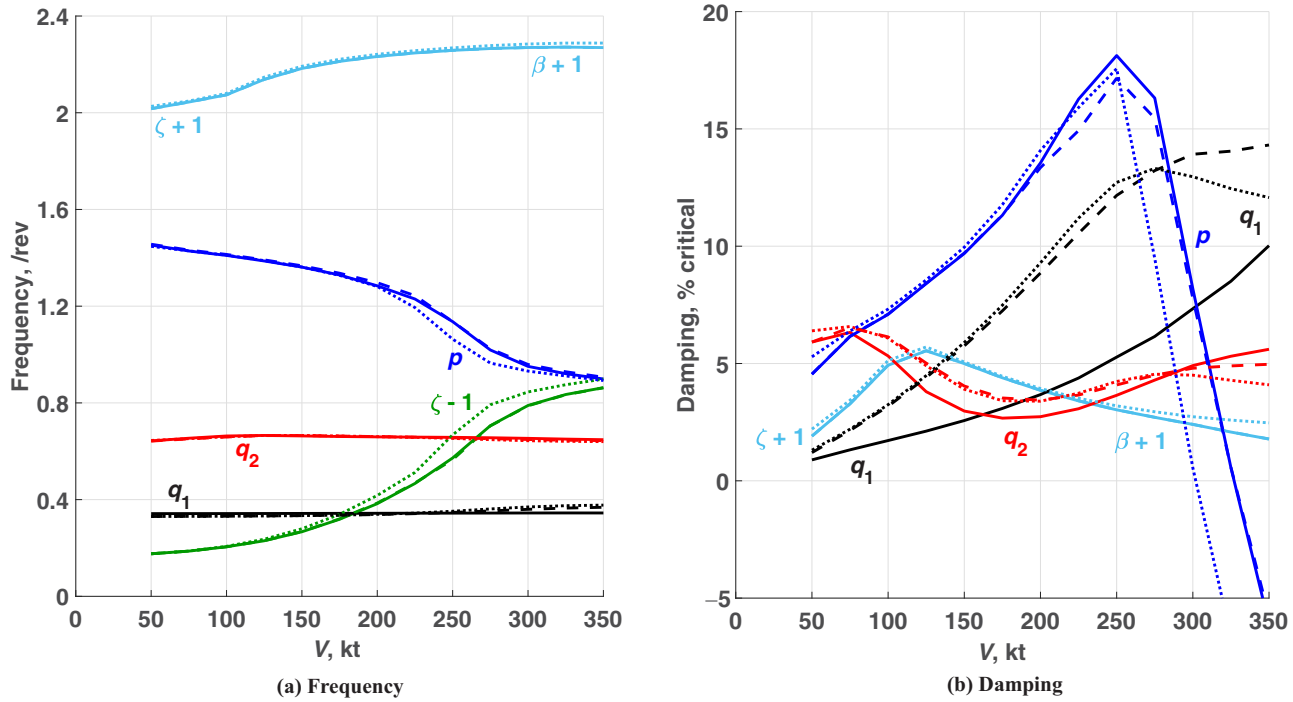

(a) Frequency (b) Damping

Fig. 12. Effect of rotor speed perturbation and powered mode operation (solid: freewheeling with rotor speed perturbation - baseline, dash: freewheeling with constant rotor speed (ideal engine), dot: powered with constant rotor speed (ideal engine)).

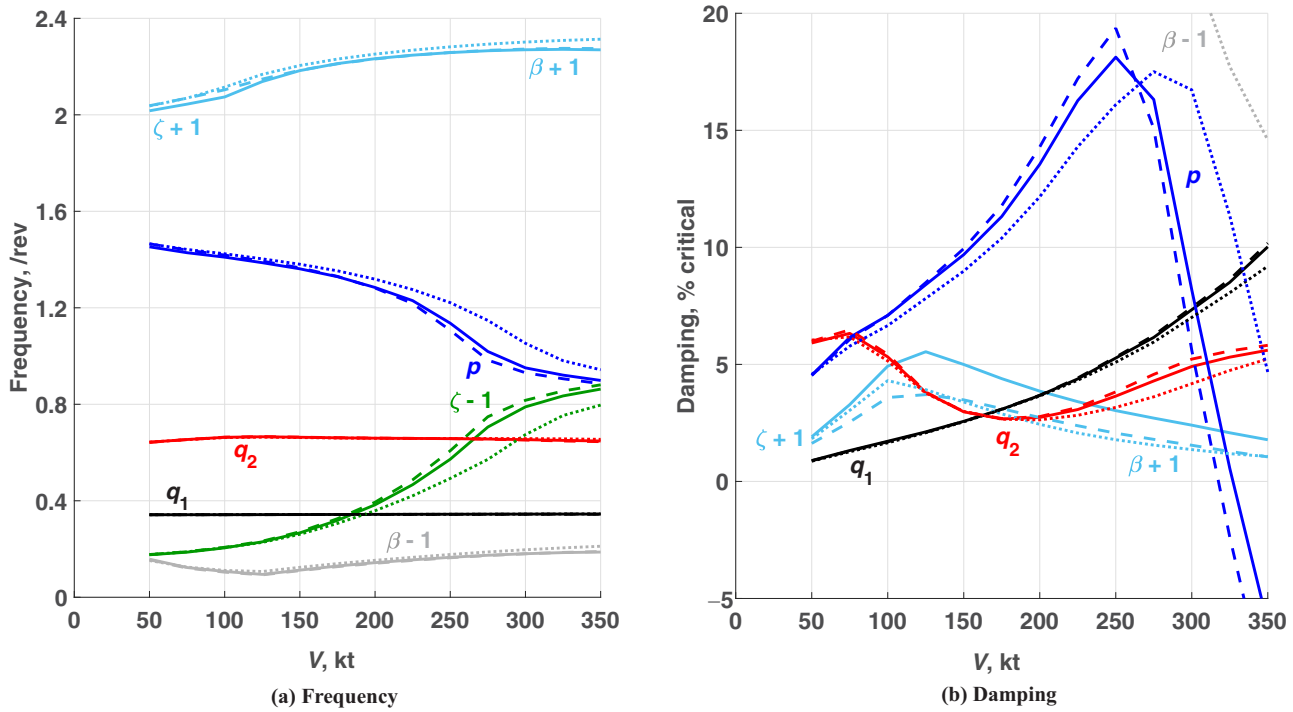

(a) Frequency (b) Damping

Fig. 13. Effect of rotor modes (solid: first 10 modes - baseline, dash: first flap, lag, and torsion modes, dot: first flap and lag modes).

if possible. But in this case where air resonance is critical, wing aerodynamics is not important at all.

To sum up, important model parameters were varied and the impact of them on the stability predictions was investigated. It was concluded that unlike loads the induced flow model bears no significance for high-speed stability. Damping predictions should be carried out for both freewheeling with rotor speed perturbation and powered modes (no perturbation) in order to find the most critical condition. At least the first rotor flap, lag, and torsion modes should be included in the analysis, but higher modes do have an effect. Linear aerodynamics for the rotor may result

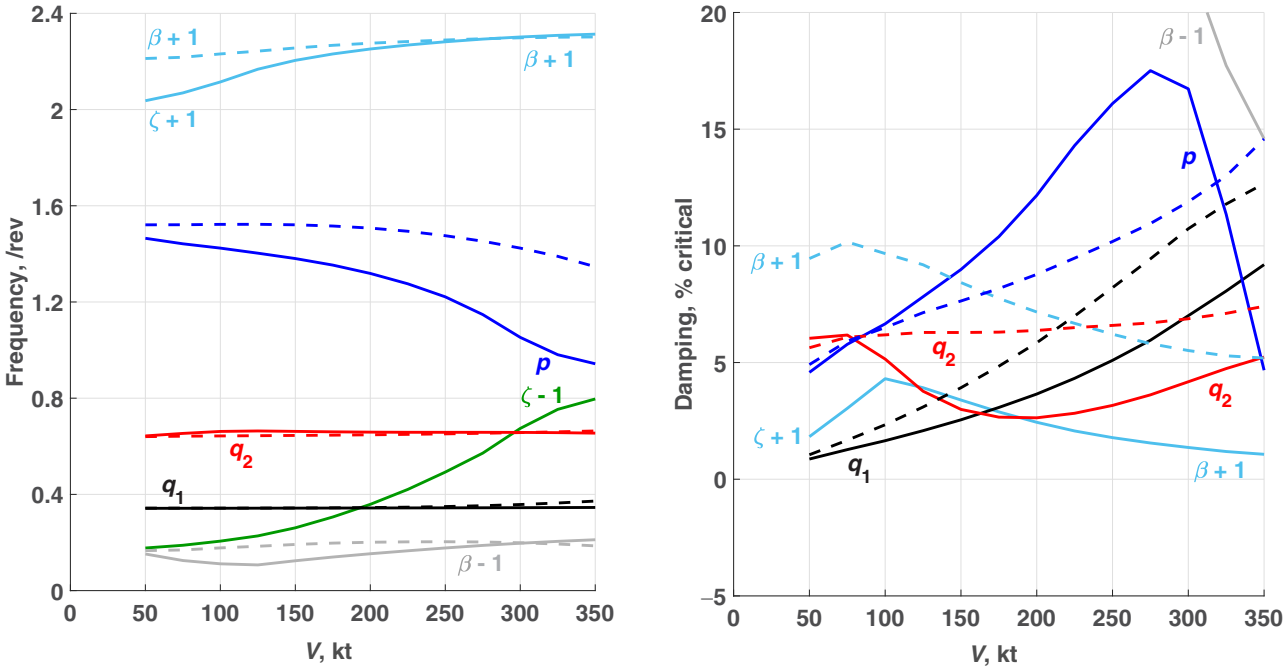

(a) Frequency (b) Damping

Fig. 14. Effect of rotor modes (solid: first flap and lag modes, dash: first flap mode only).

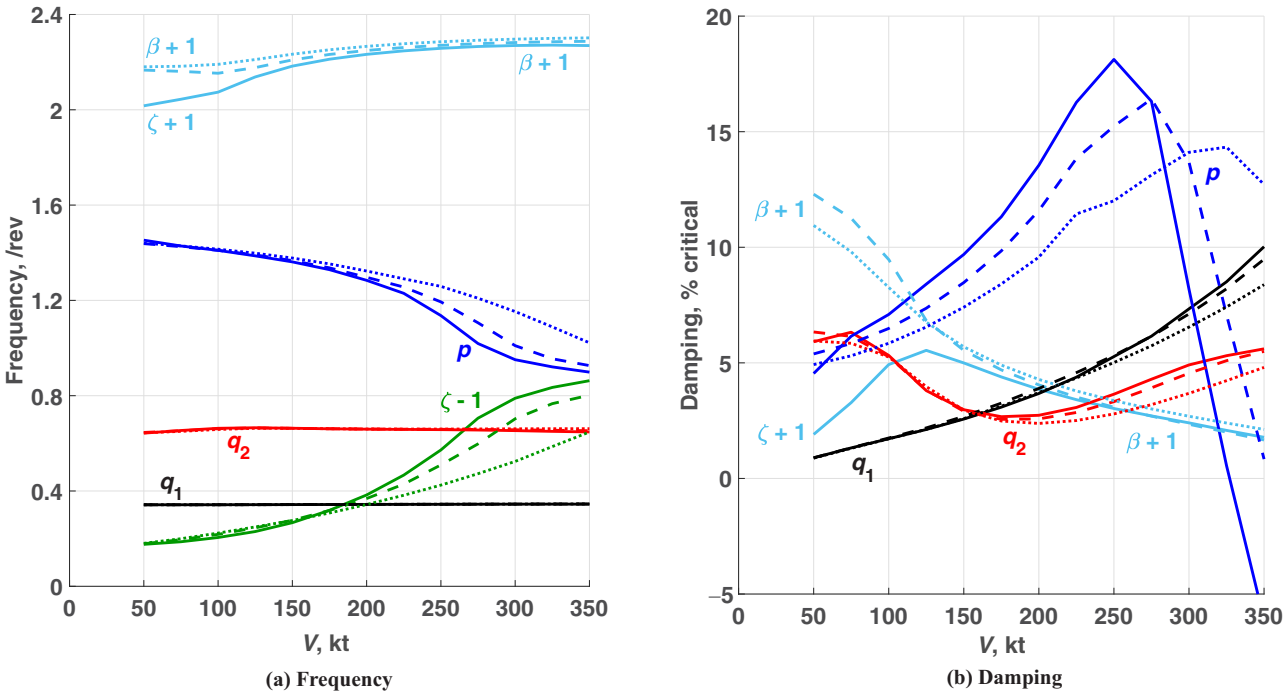

(a) Frequency (b) Damping

Fig. 15. Effect of blade airloads model (solid: C81 airfoil decks - baseline, dash: linear aerodynamics with Glauert correction, dot: incompressible linear aerodynamics).

in inaccurate predictions even with a compressibility correction; correct airfoil decks are required. The wing aerodynamic model should be taken into account also with airfoil decks, but only if q_1 is the critical mode.

Advanced Geometry Blades

There has been no previous work on advanced geometry blades for hingeless hub tiltrotors where proprotor air resonance can be the limiting

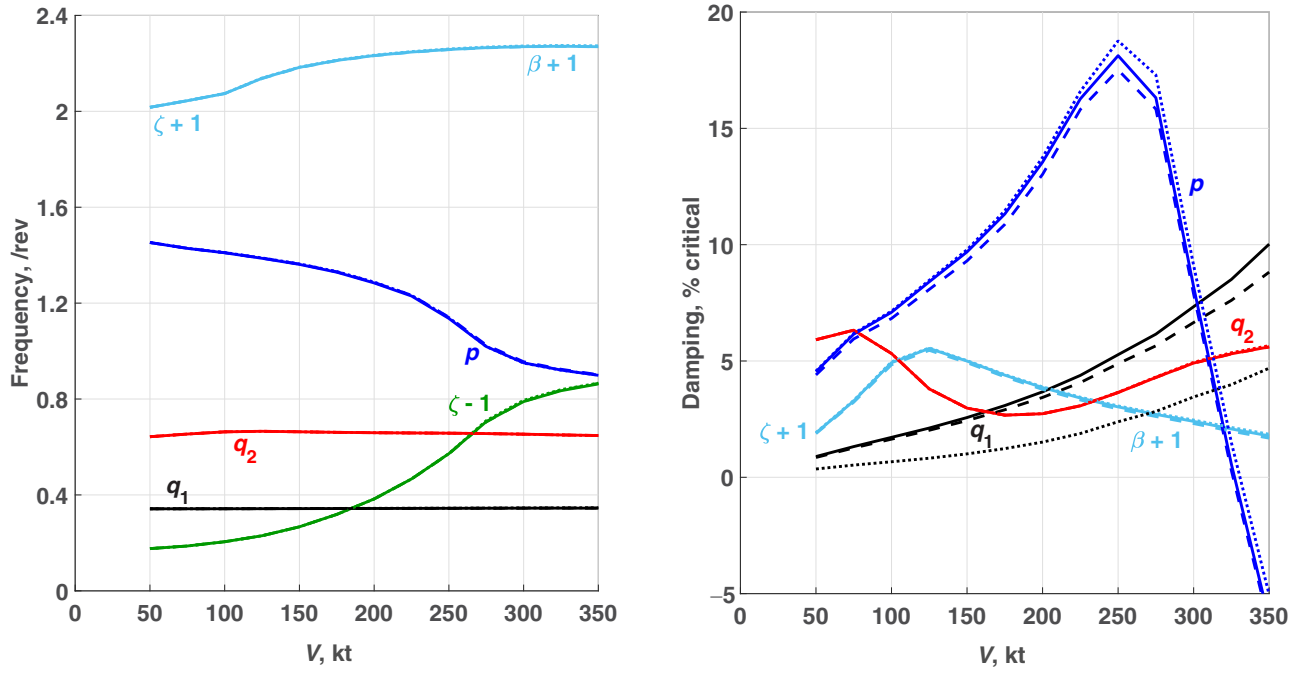

(a) Frequency (b) Damping

Fig. 16. Effect of wing aerodynamic model (solid: C81 airfoil deck - baseline, dash: incompressible linear aerodynamics, dot: no aerodynamics).

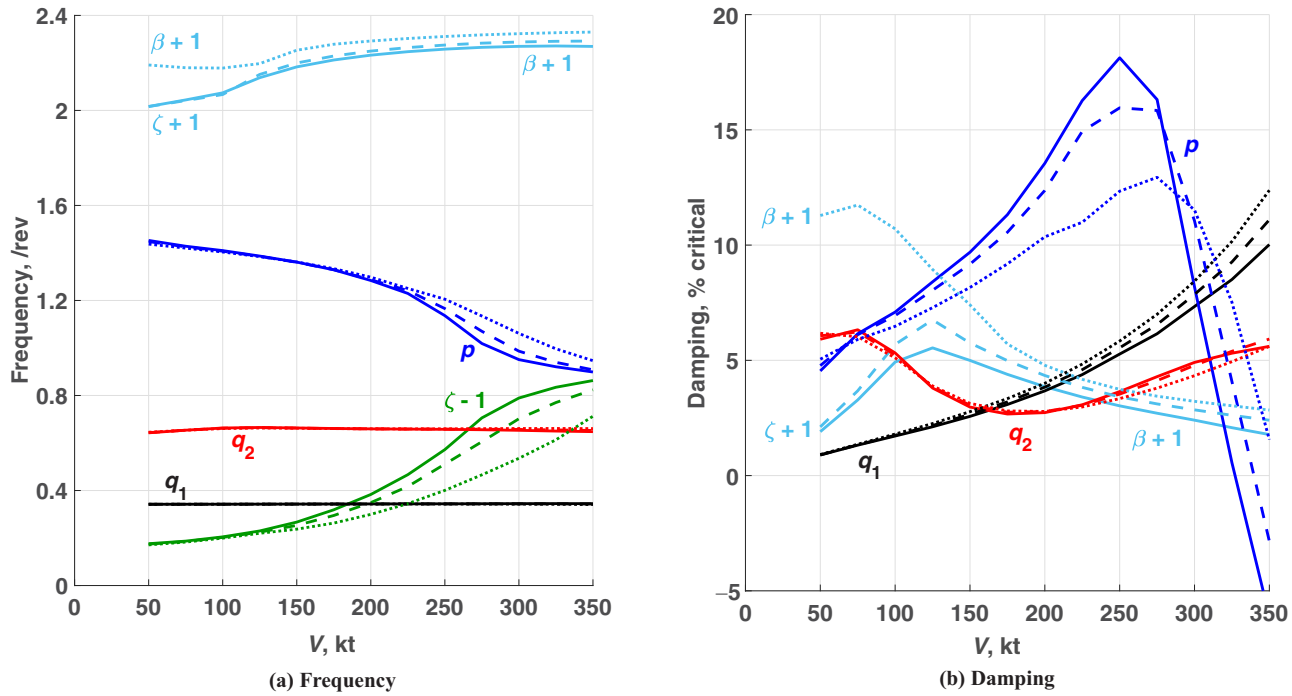

(a) Frequency (b) Damping

Fig. 17. Effect of tip sweep (solid: straight blades - baseline, dash: 10° sweep, dot: 20° sweep).

phenomenon. A few analytical studies (Refs. 15, 16, 29) undertaken were focused on gimballed hub proprotors. The objective is to determine whether tip sweep can influence the stability boundary up to 400 kt and how. Note that the wing thickness of the current model is already 13.5%; hence, it will indeed allow such speeds.

Stability

Figure 17 compares the stability roots obtained with straight and swept-tip blades. Sweep-back angles of 10° and 20° were introduced from 80%R while keeping everything else (mass, twist, chord, etc.) the

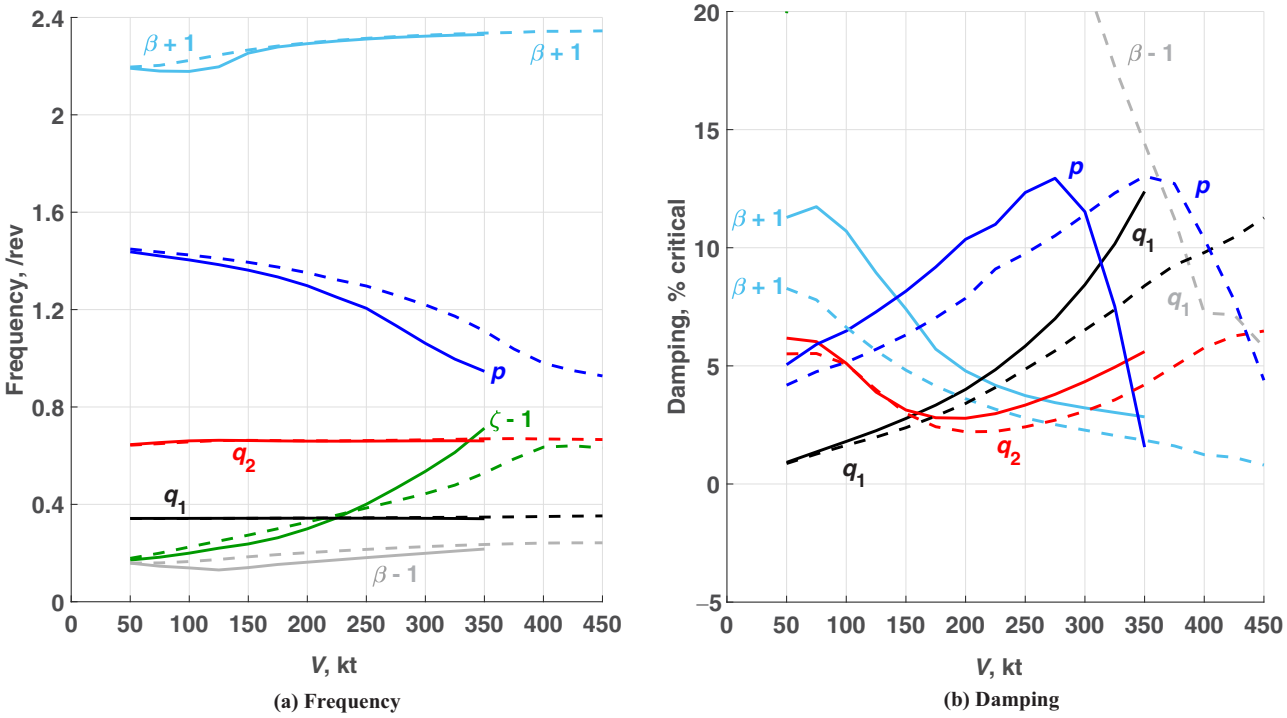

(a) Frequency (b) Damping

Fig. 18. Effect of c.g. sweep (solid: 20° sweep, dash: 20° sweep - c.g. unswept).

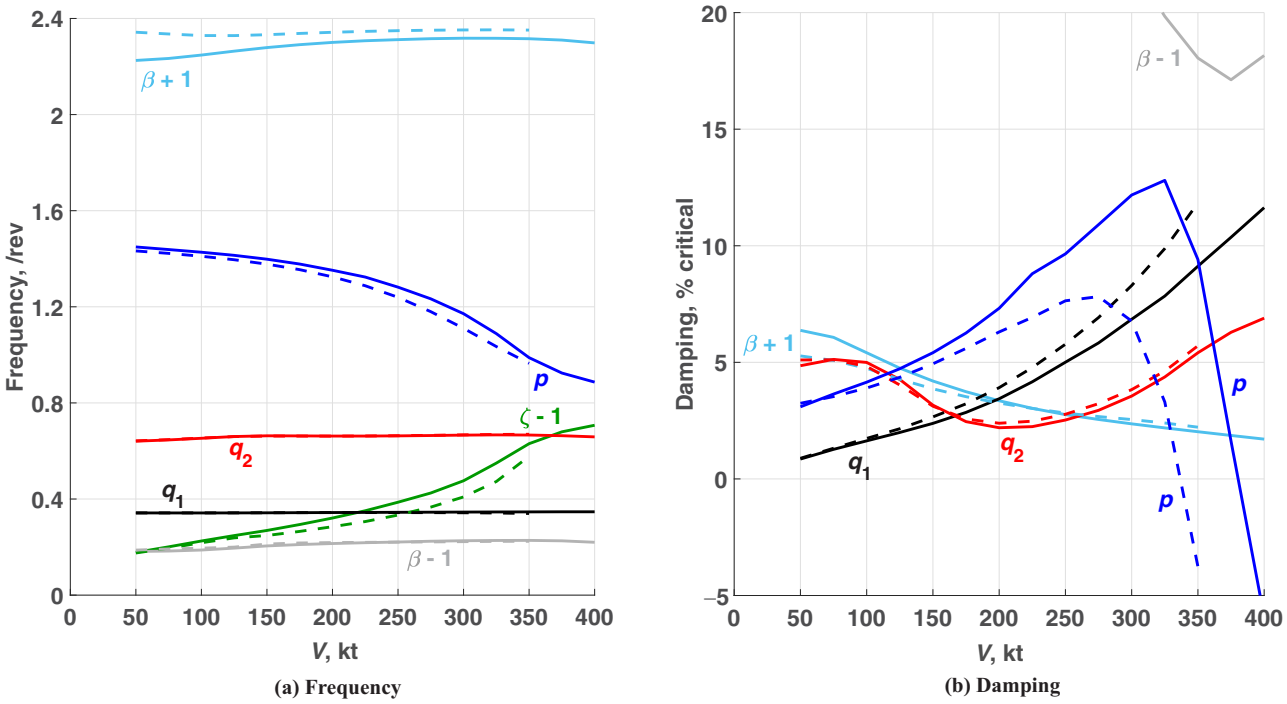

(a) Frequency (b) Damping

Fig. 19. Effect of sweep with no tip aerodynamics (solid: straight blades - baseline, dash: 20° sweep).

same. As sweep increases, damping of q_1 mode improves at high speeds but q_2 mode stays relatively unaffected. The peak damping value for the p mode decreases, but the coupling of $\zeta - 1$ and p modes is delayed at high speeds, which results in an increase in the air resonance speed for more than 10 kt with 10° sweep and more than 25 kt with 20° sweep, bringing it to near 355 kt.

Sweep introduces three changes: elastic axis, section center of gravity (c.g.), and aerodynamic center shift back. In order to examine the cause of the improvement, the section c.g. was returned back to its original unswept position in order to isolate the effect of aerodynamics alone. Figure 18 shows a comparison with the original 20° sweep case. The stability of the p mode at high speeds is significantly higher with the unswept c.g. The instability has virtually vanished up to more than 475 kt.

An additional check was performed by assuming no aerodynamic loads between 90%R and 100%R of the blade, which accounts for half

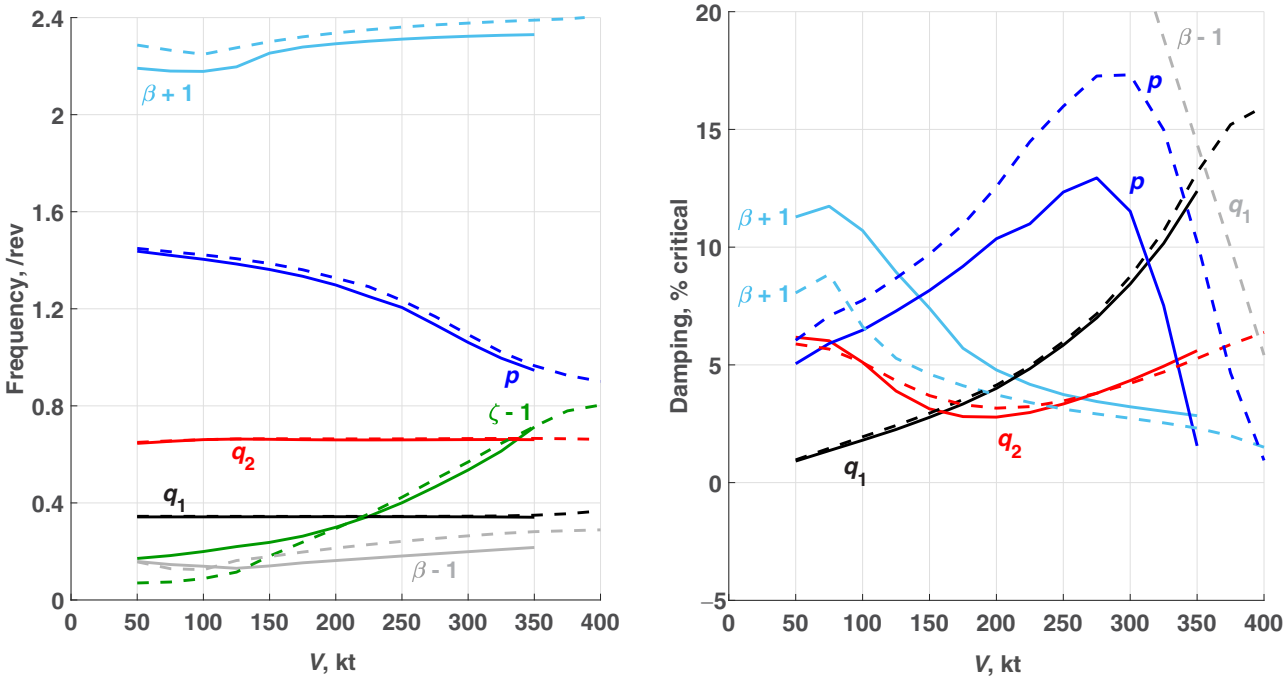

(a) Frequency (b) Damping

Fig. 20. Effect of spar in the swept region (solid: 20° sweep, dash: 20° sweep without spar).

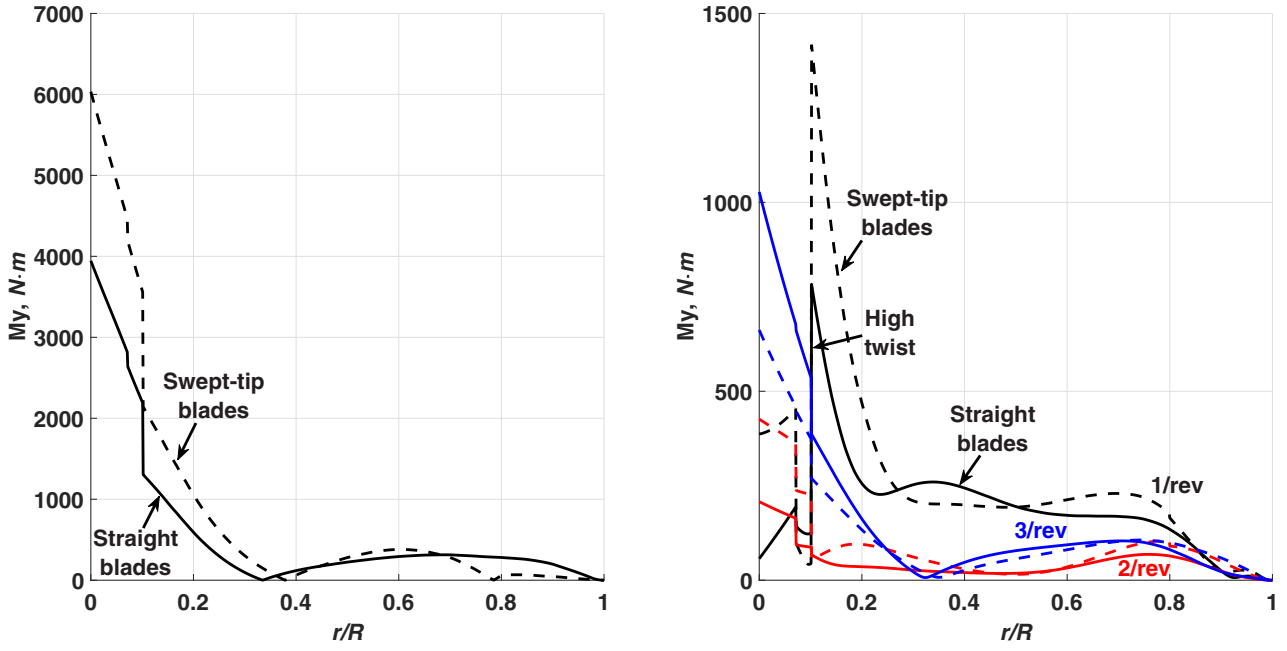

(a) Steady (b) Oscillatory

Fig. 21. Flapwise bending moment (solid: straight blades - baseline, dash: 20° sweep without spar).

of the swept area. Both baseline and 20° sweep cases were repeated and compared in Fig. 19. This time sweep decreased the air resonance speed. This is because the stabilizing effect of the aerodynamics due to sweep is not present anymore. This and the previous comparison show that the main effect is from the aerodynamic center shift, and its impact is greater than the detrimental c.g. shift back due to sweep.

This raises the question whether the stability would further improve if the swept region did not have a spar at all; this can be seen in many modern rotors. In order to mimic that, the section mass was reduced by 50% and the section c.g. was moved to 15% chord for the swept part. Figure 20 shows a comparison with the original 20° sweep results. The stability of the p mode improves, and the air resonance speed is pushed

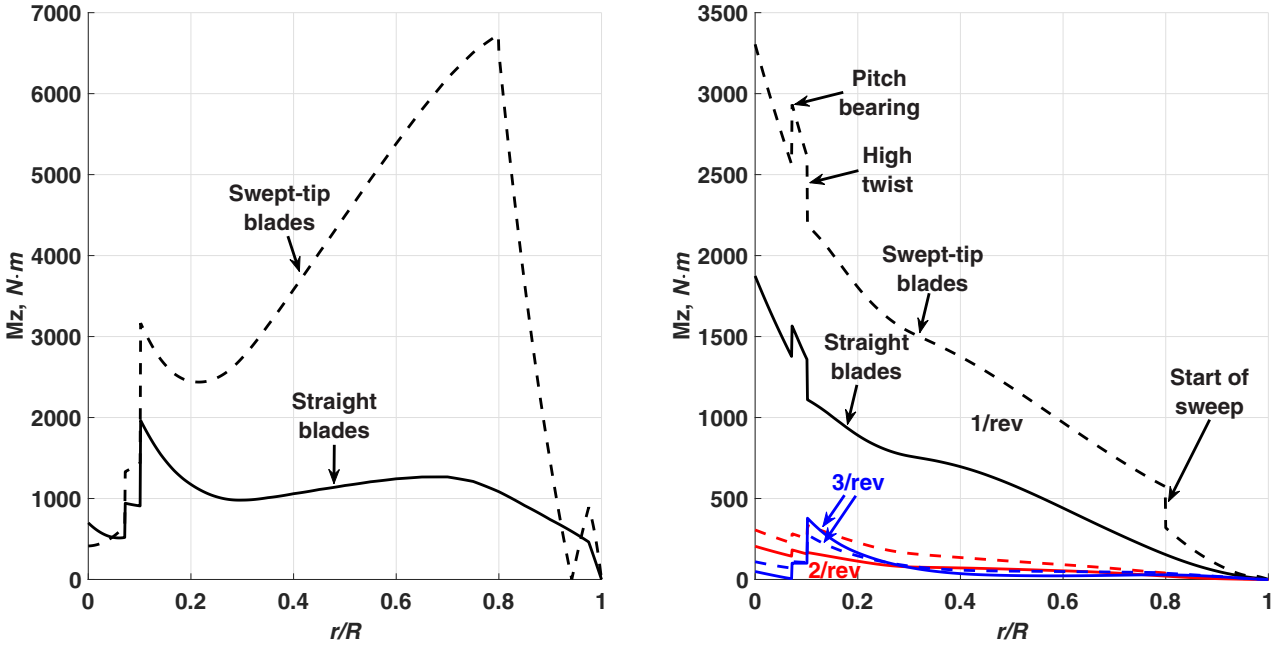

(a) Steady (b) Oscillatory

Fig. 22. Chordwise bending moment (solid: straight blades - baseline, dash: 20° sweep without spar).

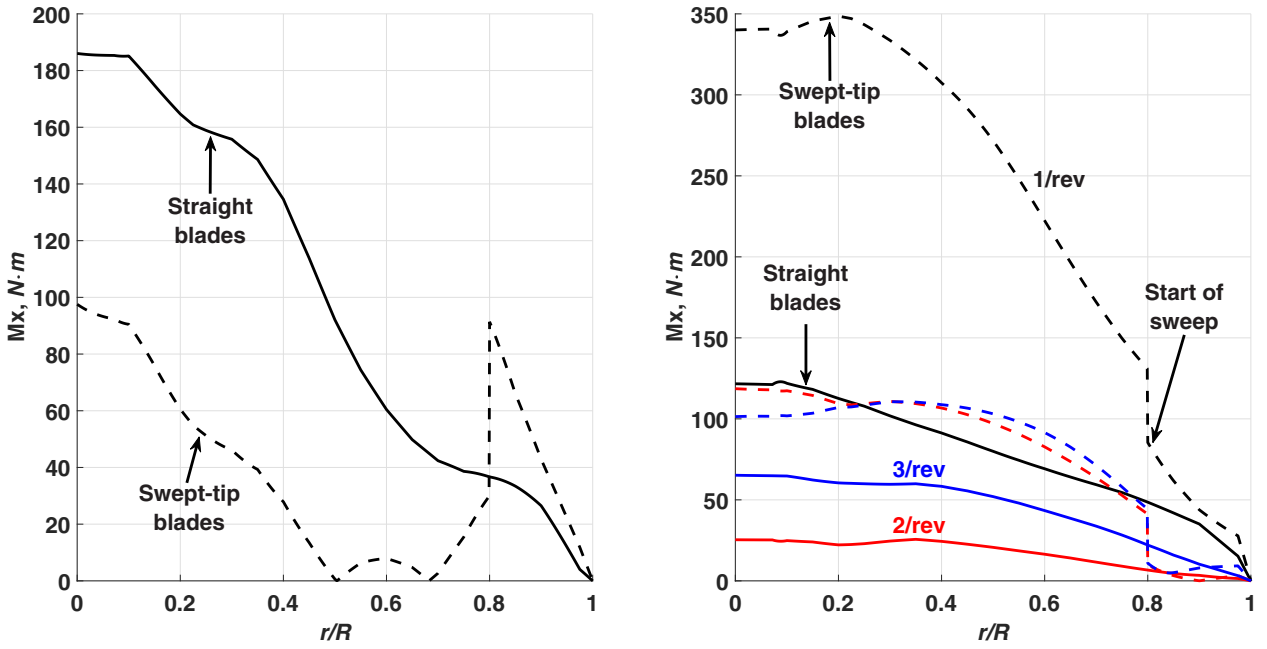

(a) Steady (b) Oscillatory

Fig. 23. Torsion moment (solid: straight blades - baseline, dash: 20° sweep without spar).

about 50 kt to near 405 kt. This, of course, does not mean the aircraft can fly at 405 kt; the instability speed should be sufficiently beyond the maximum design speed for safe flight. Compared to the straight blades, the increase in speed is more than 75 kt. Also note the rapid decrease in q_1 damping at high speed in Fig. 20. This mode starts as a $\beta-1$ mode but mostly assumes a q_1 mode shape at high speeds. This is the whirl flutter mode, and further improvements on air resonance can cause this mode to now appear as the critical one.

Loads

Loads should be monitored with the introduction of sweep as it should not introduce unacceptable blade or control loads. Figures 21–23 show the sectional steady and oscillatory flapwise, chordwise, and torsional moments in deformed frame for straight and swept-tip blades (without spar). The rotor was trimmed to zero hub moments and $C_T/\sigma = 0.12$ for a pure edgewise flight condition with $\mu = 0.15$ and $i_N = 90°$ from the flow.

The Maryland Freewake was used with a single tip vortex and a nearwake extending 30° behind. Steady, 1/rev, and 2/rev flap bending moments increase near the root with the introduction of sweep (Fig. 21). A significant change is observed in chordwise and torsional moments. Steady, 1/rev, and 2/rev chordwise moments increase along the blade and at the hub (Fig. 22). Oscillatory torsional moments also increase (Fig. 23). This would have implications for the design of the blade and the control system (pitch links, swashplate, actuators), but redesign is outside the scope of this work.

Note that the jumps in the loads are merely due to the axis system definition; each span station has a different deformed axis system (due to pitch control, sweep, twist, and deformations).

Conclusions

A new solver was built, verified, and validated systematically. Fundamental understanding of the physics of hingeless hub tiltrotor instabilities was provided. Swept-tip blades were studied in a comprehensive manner. The key conclusions are as follows:

1) Proprotor air resonance is the critical instability for Boeing M222 due to the soft in-plane hingeless hub, not whirl flutter. Air resonance occurs with the coupling of wing torsion (p) and low-frequency lag ($\zeta-1$) modes at high speeds. The mode shape is mostly lag near instability.

2) The new solver was verified with U.S. Army hypothetical case and validated with Boeing data. Air resonance predictions agreed well with the test data for low speeds. Some instabilities were not captured at high speeds; however, the behavior was predicted.

3) Induced flow bears no significance for high-speed stability predictions. Freewake is not required; a simple uniform inflow model is sufficient.

4) Predictions should be performed for both freewheeling with rotor speed perturbation and powered mode in actual flight with an ideal engine (no rotor speed perturbation) as air resonance can be more critical for the powered mode.

5) At least the first rotor flap, lag, and torsion modes must be included in the analysis.

6) Airfoil decks should be used for both the rotor and the wing. The wing aerodynamic model is only important if wing beam (q_1) mode is critical.

7) A 20° sweep back from 80%R improved instability speed by more than 75 kt, bringing it to 405 kt.

8) The aerodynamic center shift is the key mechanism; c.g. offset due to sweep is detrimental. The implication is to sweep the blade without an internal spar.

9) Whirl flutter can appear as the critical phenomenon with further improvements in the air resonance speed.

10) Steady and oscillatory chordwise and torsional moments increased significantly due to sweep. Blades and the control system may need to be redesigned with higher loads.

Future work

An interesting world of proprotor air resonance, whirl flutter, and aeroelastic loads await us in hingeless tiltrotors with a promise of near 400 kt cruise with 13.5% thick wings. Comprehensive analysis capability is ready in academia and the U.S. government to tackle this challenge. What is needed now is a set of high-quality test data. The analysis performed in this paper shed light on what to look for and how to prepare for such a test.

Acknowledgments

This work was carried out at the Alfred Gessow Rotorcraft Center, University of Maryland at College Park, under the Army/Navy/NASA Vertical Lift Research Center of Excellence (VLRCOE) grant (number W911W61120012), with technical monitor Dr. Mahendra Bhagwat and technical points of contact Dr. Hyeonsoo Yeo (U.S. Army) and Dr. Wayne Johnson (NASA Ames). We thank them for their valuable guidance on this work.

References

[1]Johnson, W., Yamauchi, G. K., and Watts, M. E., "NASA Heavy Lift Rotorcraft Systems Investigation," NASA-TP-2005-213467, 2005.

[2]Whittle, R., "Karem Aircraft Building New Tiltrotor Ideas," *Vertiflite*, Vol. 62, (1), January/February 2016, pp. 36–38.

[3]Warwick, G., "Full-Scale Single Rotor Test Advances Maturity of Karem's OSTR," *Aviation Week and Space Technology*, Vol. 182, (45), November 2020.

[4]Magee, J. P., and Alexander, H. R., "Wind Tunnel Test on a 1/4.622 Froude Scale, Hingeless Rotor, Tilt Rotor Model Volumes I-IV," NASA-CR-151936-151939, 1976.

[5]Nicely, J., and Walsh, G., "Technology Data, Operations and Maintenance Manual for a Wind Tunnel Model of a Prop Rotor and Cantilever Wing," D210-10961-1, Boeing Vertol Company, 1975.

[6]Ham, N. D., Bauer, P. H., Lawrence, T. H., and Yasue, M., "A Study of Gust and Control Response of Model Rotor-Propellers in a Wind Tunnel Airstream," NASA-CR-137756, 1975.

[7]Magee, J. P., and Alexander, H. R., "Wind Tunnel Tests of a Full Scale Hingeless Prop/Rotor Designed for the Boeing Model 222 Tilt Rotor Aircraft," NASA-CR-114664, 1973.

[8]Yeo, H., and Kreshock, A. R., "Whirl Flutter Investigation of Hingeless Proprotors," *Journal of Aircraft*, Vol. 57, (4), July–August 2020, pp. 586–596, DOI: 10.2514/1.C035609.

[9]Johnson, W., "Technology Drivers in the Development of CAMRAD II," Proceedings of the American Helicopter Society Aeromechanics Specialists' Conference, San Francisco, CA, January 1994.

[10]Johnson, W., "Rotorcraft Aeromechanics Applications of a Comprehensive Analysis," Proceedings of the American Helicopter Society International Meeting on Rotorcraft Technology and Disaster Relief, Gifu, Japan, April 1998.

[11]Saberi, H., Khoshlahjeh, M., Ormiston, R. A., and Rutkowski, M. J., "Overview of RCAS and Application to Advanced Rotorcraft Problems," Proceedings of the American Helicopter Society 4th Decennial Specialists' Conference on Aeromechanics, San Francisco, CA, January 2004.

[12]Saberi, H., Hasbun, M., Hong, J., Yeo, H., and Ormiston, R. A., "Overview of RCAS Capabilities, Validations, and Rotorcraft Applications," Proceedings of the American Helicopter Society 71st Annual Forum, Virginia Beach, VA, May 5–7, 2015.

[13]Bowen-Davies, G., "RCAS Aeromechanics Computations of the Boeing 222 Proprotor," Proceedings of the American Helicopter Society International Technical Meeting: Aeromechanics Design for Transformative Vertical Flight, San Francisco, CA, January 2018.

[14]Bowen-Davies, G., "Comparison of Vortex Wake, VVPM and CFD Aeromechanics Computations of the Boeing 222 Proprotor," Proceedings of the American Helicopter Society 74th Annual Forum, Phoenix, AZ, May 14–17, 2018.

[15]Acree, C. W., Jr., Peyran, R. J., and Johnson, W., "Rotor Design Options for Improving XV-15 Whirl-Flutter Stability Margins," NASA-TP-2004-212262, 2004.

[16]Acree, C. W., Jr.. "Effects of V-22 Blade Modifications on Whirl Flutter and Loads," *Journal of the American Helicopter Society*, Vol. 50, (3), July 2005, pp. 269–278. DOI: 10.4050/1.3092863.

[17]Bir, G., and Chopra, I., "Development of UMARC (University of Maryland Advanced Rotorcraft Code)," Proceedings of the American Helicopter Society 46th Annual Forum, Washington, DC, May 21–23, 1990.

[18]Gul, S., and Datta, A., "Development of an Aeromechanics Solver for Loads and Stability of Hingeless Tiltrotors," *Journal of Aircraft*, online published July 2022, pp. 1–17, DOI: 10.2514/1.C036944.

[19]Hodges, D. H., and Dowell, E. H., "Nonlinear Equations of Motion for the Elastic Bending and Torsion of Twisted Nonuniform Rotor Blades," NASA-TN-D-7818, 1974.

[20]Datta, A., and Chopra, I., "Validation and Understanding of UH-60A Vibratory Loads in Steady Level Flight," *Journal of the American Helicopter Society*, Vol. 49, (3), July 2004, pp. 271–287, DOI: 10.4050/JAHS.49.271.

[21]Datta, A., "Fundamental Understanding, Prediction and Validation of Rotor Vibratory Loads in Steady Level Flight," Ph.D. thesis, University of Maryland, 2004.

[22]Hodges, D. H., Ormiston, R. A., and Peters, D. A., "On the Nonlinear Deformation Geometry of Euler-Bernoulli Beams," NASA-TP-1566, 1980.

[23]Johnson, W., *Helicopter Theory*, Dover Publications, New York, NY, 1980, pp. 213–216.

[24]Johnson, W., "Dynamics of Tilting Proprotor Aircraft in Cruise Flight," NASA-TN-D-7677, 1974.

[25]He, C., and Zhao, J., "Modeling Rotor Wake Dynamics with Viscous Vortex Particle Method," *AIAA Journal*, Vol. 47, (4), April 2009, pp. 902–915, DOI: 10.2514/1.36466.

[26]Zhao, J., and He, C., "A Viscous Vortex Particle Model for Rotor Wake and Interference Analysis," *Journal of the American Helicopter Society*, **55**, 012007 (2010), DOI: 10.4050/JAHS.55.012007.

[27]Sitaraman, J., Potsdam, M., Wissink, A., Jayaraman, B., Datta, A., Mavriplis, D., and Saberi, H., "Rotor Loads Prediction Using Helios: A Multisolver Framework for Rotorcraft Aeromechanics Analysis," *Journal of Aircraft*, Vol. 50, (2), March 2013, pp. 478–492, DOI: 10.2514/1.C031897.

[28]Anon., "V/STOL Tilt Rotor Aircraft Study - Volume II: Preliminary Design of Research Aircraft," NASA-CR-114438, 1972.

[29]Srinivas, V., Chopra, I., and Nixon, M. W., "Aeroelastic Analysis of Advanced Geometry Tiltrotor Aircraft," *Journal of the American Helicopter Society*, Vol. 43, (3), July 1998, pp. 212–221, DOI: 10.4050/JAHS.43.212.